Optics Letters

Multi-spectral snapshot diffraction-based overlay metrology

Xiuguo Chen,[1,2,4] Jing Hu,[1] Wenlong Chen,[1] Shilong Yang,[1] Yifu Wang,[1] Zirong Tang,[1] and Shiyuan Liu[1,2,3]

[1]*State Key Laboratory of Digital Manufacturing Equipment and Technology, Huazhong University of Science and Technology, Wuhan 430074, China*
[2]*Optics Valley Laboratory, Wuhan 430074, China*
[3]*shyliu@hust.edu.cn*
[4]*xiuguochen@hust.edu.cn*

Diffraction-based overlay (DBO) metrology has been successfully introduced to deal with the tighter overlay control in modern semiconductor manufacturing. Moreover, DBO metrology typically needs to be performed at multiple wavelengths to achieve accurate and robust measurement in the presence of overlay target deformations. In this Letter, we outline a proposal for multi-spectral DBO metrology based on the linear relation between the overlay errors and the combinations of off-diagonal-block Mueller matrix elements $\Delta M = M_{ij} - (-1)^j M_{ji}$ ($i = 1, 2; j = 3, 4$) associated with the zeroth-order diffraction of overlay target gratings. We propose an approach that can realize snapshot and direct measurement of ΔM over a broad spectral range without any rotating or active polarization component. The simulation results demonstrate the capability of the proposed method for multi-spectral overlay metrology in a single shot.
© 2023 Optica Publishing Group

In semiconductor manufacturing, the overlay refers to the lateral displacement of a lithographically exposed and developed feature in one layer with respect to an underlying patterned layer. The measurement and control of the overlay is of vital importance to good device performance. As a rule of thumb, the maximum allowable overlay is about 1/3~1/5 of the size of the smallest feature in the integrated circuit, and the associated measurement precision is expected to be better than 1/5~1/10 of the permitted overlay error [1]. Currently, the overlay error is of the order of 1~2 nm in high-end semiconductor manufacturing, and the associated precision of overlay metrology is at the sub-nanometer level [2].

In order to deal with the tighter overlay control demands of today's semiconductor devices, diffraction-based overlay (DBO) metrology has been successfully introduced [3,4]. In DBO metrology, intensities of the +1st and −1st diffraction orders are usually collected from a specially designed target, which consists of overlapping gratings in the resist layer and an underlying layer, respectively [5,6]. The difference between the ±1st-order diffraction intensities ΔI responds approximately linearly to the shift OV between the gratings (overlay) in a small range, i.e.,

$\Delta I = K \cdot OV$, where the slope K is determined by the grating material, grating profile, and measurement configuration (the combination of wavelength, polarization, incidence angle, and azimuthal angle, etc.). To eliminate the dependence on the unknown K in practice, a pair of target gratings with the same period are designed along each direction (X and Y directions), where a small known bias of, respectively, $+d$ and $-d$ is introduced into the two target gratings. To realize better control, the overlay often needs to be measured on many points on a wafer, which requires the measurement time to be as short as possible, typically in the millisecond range [6]. Moreover, the overlay target size should be as small as possible due to the limited space reserved for the targets in the pattern on a wafer [7]. In addition, it is desired that DBO metrology tools could measure at multiple wavelengths over a broad spectral range in order to improve accuracy and robustness in the presence of overlay target deformations [8–10].

Besides the ±1st diffraction orders, the zeroth diffraction order also contains overlay information. It has been demonstrated that the combination of the off-diagonal-block Mueller matrix elements $\Delta M = M_{ij} - (-1)^j M_{ji}$ ($i = 1, 2; j = 3, 4$) associated with the zeroth diffraction order also responds approximately linearly to the overlay error OV [11–14]. Therefore, the overlay error can be measured using the zeroth-order Mueller matrix in a similar manner to the DBO technique based on the ±1st diffraction orders (see Section 1 in Supplement 1). Compared with higher diffraction orders, the zeroth-order diffraction measurement has striking advantages. First, since the zeroth-order diffraction typically has a larger intensity than higher orders, the measurement provides a better signal-to-noise ratio. Additionally, because the zeroth-order diffraction always exists for gratings with any period, smaller overlay targets can be measured. Nevertheless, the key lies in the fast collection of multi-spectral Mueller matrices.

Currently, multi-spectral Mueller matrix measurement typically adopts a temporal polarization-coding approach, where either the orientations of fast axes of the retarders vary over time, such as the dual rotating-compensator Mueller matrix ellipsometer (MME) [15], or the retardances of the retarders vary over time, such as the MME with four liquid-crystal variable retarders [16] or with four photoelastic modulators [17]. However, the

measurement time for the Mueller matrices in a broad spectral range often takes several seconds at least. In comparison, the spectral polarization-coding approach relies on a property that the retardances of some multi-order birefringent crystals—such as quartz, MgF_2, and calcite—change approximately linearly with the wavenumber (reciprocal of the wavelength) in the visible to near-infrared band. The above multi-order birefringent retarders encode polarization information into the intensity spectrum without any rotating or active polarization component, and then we can perform Fourier analysis to decode the polarization parameters from the modulated spectrum [18]. Consequently, multi-spectral Mueller matrix measurement can be realized in a single integration interval of the detector (thus also termed the snapshot measurement), which could reach up to 10 ns according to a recent report [19].

In this Letter, we propose an approach to directly achieve the combination of the off-diagonal-block Mueller matrix elements ΔM in a broad spectral range based on the spectral polarization-coding technique. So far, the snapshot Mueller matrix measurement is usually realized by employing four multi-order retarders, i.e., two in the polarization state generator (PSG) and another two in the polarization state analyzer (PSA), with a proper thickness ratio and proper orientations of the fast axes [20,21]. Although the full 4×4 Mueller matrix can be obtained with the above configuration of the four multi-order retarders, the measurement process typically involves more than 20 frequency channels. The cross talk between adjacent frequency channels greatly restricts its applications in broadband measurement and also affects the measurement accuracy of Mueller matrix elements. In comparison, there are only two multi-order retarders in our method (one in the PSG and another in the PSA). By choosing a proper thickness ratio of the two multi-order retarders as well as proper orientations of their fast axes, the combination of the off-diagonal-block Mueller matrix elements ΔM can be directly achieved with only five frequency channels. Fewer frequency channels makes our method suitable for more accurate measurement in a broader spectral range.

Working principle. Figure 1 presents the basic system layout for the snapshot measurement of combinations of the
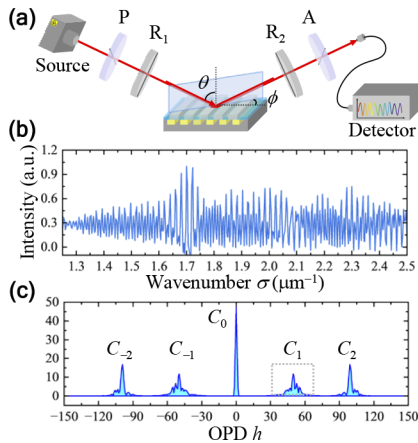

Fig. 1. (a) Schematic of the basic system layout for the snapshot measurement of combinations of the off-diagonal-block Mueller matrix elements, where θ and ϕ denote the incidence and azimuthal angles, respectively; (b) collected intensity spectrum; and (c) channel structure obtained by taking the Fourier transform of the intensity spectrum.

off-diagonal-block Mueller matrix elements. The light from a broadband source passes successively through the polarizer (P), the first multi-order retarder (R_1), and then illuminates the sample (i.e., the overlay target grating). The diffracted light from the sample then passes successively through the second multi-order retarder (R_2), the analyzer (A), and finally enters into the detector, which could be a spectrometer or an imaging spectrometer. Other optical components, such as different kinds of lenses used for beam collimation and convergence, are omitted here for brevity. According to Fig. 1, the system model in terms of the Stokes–Mueller formalism can be expressed as

$$\boldsymbol{S}_{\text{out}} = [\mathbf{M}_A \mathbf{R}(\alpha_2)][\mathbf{R}(-\beta_2)\mathbf{M}_R(\delta_2)\mathbf{R}(\beta_2)]\mathbf{M}_S \\ [\mathbf{R}(-\beta_1)\mathbf{M}_R(\delta_1)\mathbf{R}(\beta_1)][\mathbf{R}(-\alpha_1)\mathbf{M}_P]\boldsymbol{S}_{\text{in}}, \tag{1}$$

where $\mathbf{M}_S$ represents the sample Mueller matrix; $\mathbf{M}_P$ and $\mathbf{M}_A$ denote the Mueller matrices of the polarizer and analyzer, respectively; $\mathbf{M}_R(\delta_1)$ and $\mathbf{M}_R(\delta_2)$ are the Mueller matrices of the first and second multi-order retarders with retardances of δ_1 and δ_2, respectively; $\mathbf{R}(\cdot)$ represents the Mueller rotation transformation matrix; α_1 and α_2 are the transmission-axis orientations of the polarizer and analyzer, respectively; β_1 and β_2 are fast-axis orientations of the two retarders; $\boldsymbol{S}_{\text{in}} = [I_{\text{in}}, 0, 0, 0]^T$ represents the Stokes vector of the incident light with an intensity of I_{in}; and $\boldsymbol{S}_{\text{out}}$ is the corresponding Stokes vector of the diffracted light.

The wavenumber-dependent phase retardance of the multi-order retarder can be expressed as [18]

$$\delta(\sigma) = 2\pi t B(\sigma)\sigma \approx 2\pi f_0 \sigma, \tag{2}$$

where σ is the wavenumber; t and $B(\sigma)$ represent the thickness and birefringence of the retarder, respectively; and $f_0 = \frac{1}{2\pi}\frac{d\delta}{d\sigma}\big|_{\sigma=\sigma_0}$, with σ_0 being the central wavenumber. If we let $\delta_1 = \delta_2 = \delta$, $\alpha_1 = \alpha_2 = 45°$, and $\beta_1 = \beta_2 = 90°$ in Eq. (1), by multiplying the matrices in Eq. (1), we can obtain the irradiance spectrum at the detector as follows:

$$I_{\text{out}}(\sigma) = \frac{1}{4}I_{\text{in}}(\sigma)\bigg\{M_{11} + \frac{1}{2}(M_{33} - M_{44}) + \\ \frac{1}{2}[(M_{13} + M_{31}) + i(M_{41} - M_{14})]e^{i\delta(\sigma)} + \frac{1}{2}[(M_{13} + M_{31}) - i(M_{41} - M_{14})]e^{-i\delta(\sigma)} + \\ \frac{1}{4}[(M_{33} + M_{44}) + i(M_{43} - M_{34})]e^{i2\delta(\sigma)} + \frac{1}{4}[(M_{33} + M_{44}) - i(M_{43} - M_{34})]e^{-i2\delta(\sigma)}\bigg\}, \tag{3}$$

where M_{ij} ($i, j = 1, 2, 3, 4$) denotes the sample Mueller matrix elements. After substituting Eq. (2) into Eq. (3), we can see that the combinations of the sample Mueller matrix elements, especially the combinations of the off-diagonal-block Mueller matrix elements $M_{13} + M_{31}$ and $M_{41} - M_{14}$, are modulated into different frequency channels in the Fourier domain as follows:

$$C_i(h) = \mathcal{F}\{I_{\text{out}}(\sigma)\} \cdot W_i(h), \tag{4}$$

where i ($i = 0, \pm 1, \pm 2$) is the channel number, h is the optical path difference (OPD), $\mathcal{F}\{\cdot\}$ denotes the Fourier transform, and $W_i(h)$ is a rectangular windowing function. The window width of $W_i(h)$ is generally less than the channel spacings and greater than the bandwidth of sample signal in the OPD domain. Since $\delta_1 = \delta_2 = \delta$, the channel spacings between adjacent channels are equal and given by $\Delta h = [\delta(\sigma_{\text{max}}) - \delta(\sigma_{\text{min}})]/[2\pi(\sigma_{\text{max}} - \sigma_{\text{min}})]$. Note that too wide a window width will introduce additional random noise, while too narrow a window width will exclude effective sample information. The combinations of off-diagonal-block Mueller matrix elements $M_{13} + M_{31}$ and $M_{41} - M_{14}$ can
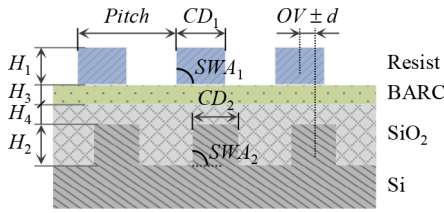
Fig. 2. Schematic of the overlay target grating.

Fig. 3. Comparison between the theoretical and recovered spectra of $M_{13} + M_{31}$ and $M_{41} - M_{14}$ for the two target gratings: (a) $OV + d$ and (b) $OV - d$ at the incidence angle of $\theta = 65°$ and azimuthal angle of $\phi = 90°$, where the overlay error was set to be $OV = 5$ nm; and (c) and (d) the corresponding recovery errors.

then be acquired by taking the inverse Fourier transform of the channels in the OPD domain as

$$M_{13} + M_{31} = \mathrm{Re}\{8\mathcal{F}^{-1}\{C_1(h)\}e^{-\mathrm{i}\delta(\sigma)}\}/I_{\mathrm{in}}(\sigma), \quad \textbf{(5a)}$$

$$M_{41} - M_{14} = \mathrm{Im}\{8\mathcal{F}^{-1}\{C_1(h)\}e^{-\mathrm{i}\delta(\sigma)}\}/I_{\mathrm{in}}(\sigma), \quad \textbf{(5b)}$$

where $\mathrm{Re}\{\cdot\}$ and $\mathrm{Im}\{\cdot\}$ represent the real and imaginary parts of a complex number, respectively.

Compared with the traditional snapshot full Mueller matrix polarimetry, which typically involves more than 20 frequency channels in measurement [20,21], as presented in Eq. (3), the proposed method only involves five channels and thus is more suitable for broadband measurement with a loose requirement on spectral resolution of the detector. It is noted that, besides the configuration of $\delta_1 = \delta_2 = \delta$, $\alpha_1 = \alpha_2 = 45°$, and $\beta_1 = \beta_2 = 90°$, there are some other configurations that can also be used for the snapshot measurement of combinations of off-diagonal-block Mueller matrix elements (see Section 2 in Supplement 1). In addition, we analyze the measurement results of combinations of the off-diagonal-block Mueller matrix elements in the presence of alignment errors in orientations of the polarization components (see Section 3 in Supplement 1). We find that the real part of $C_1(h)$ contains contributions from not only $M_{13} + M_{31}$ but also the elements M_{12}, M_{21}, M_{23}, and M_{32} in the presence of alignment errors. Meanwhile, the imaginary part of $C_1(h)$ contains contributions from both $M_{41} - M_{14}$ and elements M_{24} and M_{42}. Considering that the elements M_{12} and M_{21} are generally not equal to zero at any azimuthal configurations of the target grating, which will ultimately lead to a nonzero intercept in the linear relation for overlay metrology and affect the measurement accuracy of overlay errors, the imaginary part of $C_1(h)$ thereby seems to be better than its real part.

Results and discussion. Figure 2 depicts the schematic of the overlay target grating investigated in the simulation. The materials from top to bottom are photoresist (Resist), bottom anti-reflective coating (BARC), silicon dioxide (SiO_2), and silicon (Si). The pitch of the target grating is 400 nm. We assume that the target grating has a symmetrical profile. The critical dimension (CD), height, and sidewall angle (SWA) of the top photoresist grating are $CD_1 = 200$ nm, $H_1 = 110$ nm, and $SWA_1 = 87°$, respectively. The CD, height, and SWA of the bottom Si grating are $CD_2 = 140$ nm, $H_2 = 150$ nm, and $SWA_2 = 87°$, respectively. The thicknesses of the middle BARC and SiO_2 layers are $H_3 = 15$ nm and $H_4 = 100$ nm, respectively. The intentional bias of the target grating was set to be $d = 10$ nm.

In the simulation, the materials of the two multi-order retarders R_1 and R_2 in Fig. 1 were chosen to be MgF_2 due to the good linearity of the retardance of MgF_2 with respect to wavenumber in the visible to near-infrared band [22]. The thicknesses of the two multi-order retarders R_1 and R_2 were chosen to be $t = 6.4$ mm. The relation between the thicknesses of the multi-order retarders and the spectral resolution of the detector can be
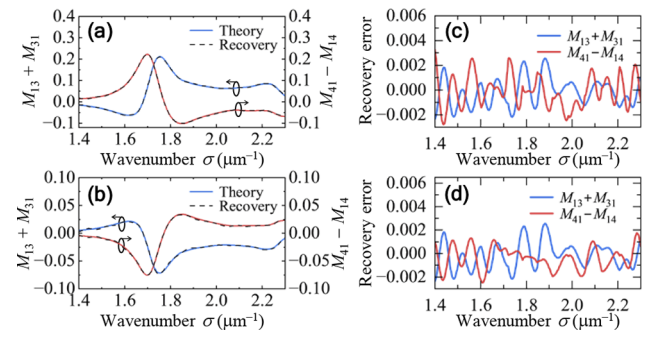
determined according to the sampling theorem (see Section 4 in Supplement 1). Rigorous coupled-wave analysis (RCWA) [23] was adopted to calculate the zeroth-order Mueller matrices of the target grating at different measurement configurations. To simulate the detection noise, Gaussian random noise was added to the intensity spectrum $I_{\mathrm{out}}(\sigma)$ calculated by Eq. (3) with a standard deviation of 1% of $I_{\mathrm{out}}(\sigma)$ (about 40 dB). Averaging the simulated intensity spectra multiple times can mimic different exposure time settings of the detector in practice. We averaged the simulated intensity spectrum ten times in the simulation. For the above overlay target grating and thickness setting of the two multi-order retarders, we found that a window width of $\Delta h/3$ was appropriate for accurate recovery of $M_{13} + M_{31}$ and $M_{41} - M_{14}$ from the intensity spectrum by simulation.

Figure 3 presents the comparison between the recovered and the RCWA-calculated theoretical spectra of $M_{13} + M_{31}$ and $M_{41} - M_{14}$ for the two target gratings ($OV + d$ and $OV - d$) at the incidence angle of $\theta = 65°$ and azimuthal angle of $\phi = 90°$. The recovery results at other measurement configurations are presented in Fig. S3 in Supplement 1. As can be observed, the recovered spectra exhibit good agreement with the theoretical spectra within a broad spectral range from about 430 nm to 710 nm. The recovery errors defined as the differences between the recovered and theoretical spectra are mainly attributed to the random noise in the intensity spectrum, the recovery algorithm, and the actual nonlinear dispersion of the retardance of MgF_2 [22].

The recovered combinations of the off-diagonal-block Mueller matrix elements $M_{13} + M_{31}$ and $M_{41} - M_{14}$ were then used to measure overlay errors (see Section 1 in Supplement 1 for the measurement principle). Figure 4 presents the comparison between the preset (input) and the measured overlay errors from the recovered $M_{13} + M_{31}$ and $M_{41} - M_{14}$ spectra at $\theta = 65°$
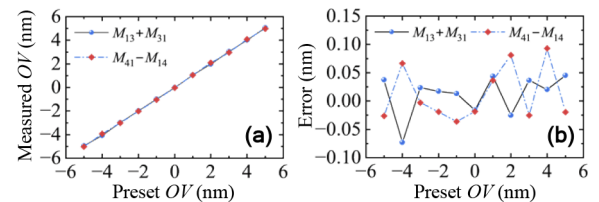

Fig. 4. (a) Comparison between the preset and measured overlay errors from the $M_{13} + M_{31}$ and $M_{41} - M_{14}$ spectra, and (b) the corresponding measurement errors.

and $\phi = 90°$. Although a single wavelength value of $M_{13} + M_{31}$ or $M_{41} - M_{14}$ was enough to measure overlay errors, we averaged the values of $M_{13} + M_{31}$ and $M_{41} - M_{14}$ over a randomly selected spectral range from about 500 nm to 550 nm and then used the averaged value to measure overlay errors to demonstrate the capability of our proposed method for multi-spectral overlay metrology. Note that the above multi-wavelength averaging also improves measurement accuracy of overlay errors (see Fig. S5 in Supplement 1). The measurement results of overlay errors at other measurement configurations are presented in Fig. S4 in Supplement 1. As can be observed, the measured overlay errors from $M_{13} + M_{31}$ and $M_{41} - M_{14}$ both show good agreement with the corresponding preset values. Higher measurement accuracy of overlay errors could be achieved if we further average the measured results from $M_{13} + M_{31}$ and $M_{41} - M_{14}$.

The results presented in Figs. 3 and 4, as well as in Figs. S3 and S4 in Supplement 1, clearly demonstrate the capability of the proposed method for multi-spectral overlay metrology in a single shot. In the above simulation, the source intensity I_{in} was assumed to be constant with wavelength. We should note that in practice, I_{in} will not only vary with wavelength but also fluctuate over time. The accurate calibration of I_{in} is thereby of importance for the accurate recovery of Mueller matrix elements and measurement of overlay errors. In addition, attention should be paid to the retardances of multi-order retarders which are susceptible to ambient temperature [24].

Conclusion. We have proposed an approach for the snapshot and direct measurement of combinations of off-diagonal-block Mueller matrix elements associated with the zeroth-order diffraction of overlay target gratings. The simulation results have demonstrated the capability of the proposed method for multi-spectral overlay metrology in a single shot. Due to the compact size in polarization modulation and demodulation, the proposed method can be further combined with angle-resolved scatterometry based on a high-numerical-aperture objective [5] by replacing the detector with an imaging spectrometer to achieve snapshot measurement at multiple wavelengths, multiple incidence angles, and multiple azimuthal angles for more accurate and robust overlay metrology. It should be pointed out that this work is a report of the first step of the research where the proposal and preliminary verification of the proposed method in realizing multi-spectral snapshot overlay metrology were primarily focused. The combination of the proposed method with angle-resolved scatterometry will be investigated in the next step of our research. In addition, the exploration of the collected multi-spectral Mueller matrix elements for accurate and robust overlay measurement in the presence of target deformations will be carried out as future work, which involves the optimization of target designs [25] and measurement configurations [26].

Disclosures. The authors declare no conflicts of interest.

Data availability. Data underlying the results presented in this paper are not publicly available at this time but may be obtained from the authors upon reasonable request.

Supplemental document. See Supplement 1 for supporting content.

REFERENCES

1. B. W. Smith and K. Suzuki, *Microlithography Science and Technology*, 3rd ed. (CRC Press, 2020), Chap. 12.
2. "International roadmap for devices and systems (IRDS), metrology (Table MET-3)," (IEEE, 2022). https://irds.ieee.org.
3. W. Yang, R. Lowe-Webb, S. Rabello, J. Hu, J. Y. Lin, J. Heaton, M. Dusa, A. den Boef, M. van der Schaar, and A. Hunter, Proc. SPIE **5038**, 200 (2003).
4. M. Adel, D. Kandel, V. Levinski, J. Seligson, and A. Kuniavsky, Proc. SPIE **6922**, 692202 (2008).
5. A. J. den Boef, Surf. Topogr.: Metrol. Prop. **4**, 023001 (2016).
6. C. Messinis, T. T. M. van Schaijk, N. Pandey, V. T. Tenner, S. Witte, J. F. de Boer, and A. den Boef, Opt. Express **28**, 37419 (2020).
7. V. Calado, J. Dépré, C. Massacrier, S. Tarabrin, R. van Haren, F. Dettoni, R. Bouyssou, and C. Dezauzier, Proc. SPIE **10585**, 6 (2018).
8. K. Bhattacharyya, A. den Boef, G. Storms, J. van Heijst, M. Noot, K. An, N. K. Park, S. R. Jeon, N. L. Oh, E. McNamara, F. van de Mast, S. H. Oh, S. Y. Lee, C. Hwang, and K. Lee, Proc. SPIE **9778**, 97781I (2016).
9. S. Mathijssen, M. Noot, M. Bozkurt, N. Javaheri, R. Hajiahmadi, A. Zagaris, K. Chang, B. Gosali, E. Su, C. Wang, A. den Boef, K. Bhattacharyya, G. T. Huang, K. H. Chen, and J. Lin, Proc. SPIE **10959**, 50 (2019).
10. J. Kim, J. Lee, C. Hwang, S. Y. Lee, W. Jung, J. Park, K. Bhattacharyya, A. den Boef, S. Mathijssen, M. Noot, F. Farhadzadeh, D. Park, K. Padhye, S. R. Jeon, S. B. Yang, W. J. Jang, and O. S. Kwon, Proc. SPIE **11325**, 44 (2020).
11. T. Novikova, A. De Martino, R. Ossikovski, and B. Drévillon, Eur. Phys. J. Appl. Phys. **31**, 63 (2005).
12. Y. N. Kim, J. S. Paek, S. Rabello, S. Lee, J. Hu, Z. Liu, Y. Hao, and W. McGahan, Opt. Express **17**, 21336 (2009).
13. C. Fallet, T. Novikova, M. Foldyna, S. Manhas, B. H. Ibrahim, A. De Martino, C. Vannuffel, and C. Constancias, J. Micro/Nanolith. MEMS MOEMS **10**, 033017 (2011).
14. X. Chen, H. Gu, H. Jiang, C. Zhang, and S. Liu, Opt. Express **25**, 8491 (2017).
15. R. M. A. Azzam, Opt. Lett. **2**, 148 (1978).
16. A. De Martino, Y. K. Kim, E. Garcia-Caurel, B. Laude, and B. Drévillon, Opt. Lett. **28**, 616 (2003).
17. O. Arteaga, J. Freudenthal, B. Wang, and B. Kahr, Appl. Opt. **51**, 6805 (2012).
18. K. Oka and T. Kato, Opt. Lett. **24**, 1475 (1999).
19. Y. Feng, J. Huang, J. Zhou, S. Gao, W. Liu, X. Jiang, S. Huang, and Z. Li, Opt. Lett. **47**, 1403 (2022).
20. N. Hagen, K. Oka, and E. L. Dereniak, Opt. Lett. **32**, 2100 (2007).
21. M. Dubreuil, S. Rivet, B. Le Jeune, and J. Cariou, Opt. Express **15**, 13660 (2007).
22. N. Hagen, P. Buranasiri, and Y. Otani, Appl. Opt. **59**, 5032 (2020).
23. M. G. Moharam, E. B. Grann, D. A. Pommet, and T. K. Gaylord, J. Opt. Soc. Am. A **12**, 1068 (1995).
24. B. D. Chrysler, K. Oka, Y. Otani, and N. Hagen, Appl. Opt. **59**, 9424 (2020).
25. Y. Shi, K. Li, X. Chen, P. Wang, H. Gu, H. Jiang, C. Zhang, and S. Liu, Appl. Opt. **59**, 2897 (2020).
26. H. C. Hsieh, J. M. Cheng, and Y. C. Yeh, Appl. Opt. **61**, 1389 (2022).

Optics Letters

Multi-spectral snapshot diffraction-based overlay metrology: supplement

XIUGUO CHEN,[1,2,4,] (iD) JING HU,[1] WENLONG CHEN,[1] SHILONG YANG,[1] YIFU WANG,[1] ZIRONG TANG,[1] AND SHIYUAN LIU[1,2,3] (iD)

[1] *State Key Laboratory of Digital Manufacturing Equipment and Technology, Huazhong University of Science and Technology, Wuhan 430074, China*
[2] *Optics Valley Laboratory, Wuhan 430074, China*
[3] *shyliu@hust.edu.cn*
[4] *xiuguochen@hust.edu.cn*

Multi-spectral snapshot diffraction-based overlay metrology: supplemental document

1. Overview of DBO metrology based on the zeroth-order Mueller matrix

The overlay metrology using the zeroth-order Mueller matrix is based on an empirical linear relation, that is, the combination of the off-diagonal-block Mueller matrix elements ΔM associated with the zeroth-order diffraction of the overlay target grating is approximately linear with respect to the overlay error OV when OV is in a small range, i.e.,

$$\Delta M = M_{ij} - (-1)^j M_{ji} \approx K \cdot OV \quad (i = 1, 2; j = 3, 4) . \tag{S1}$$

As schematically shown in Fig.S1, to realize overlay metrology, two target gratings with the same period are designed along each direction (X or Y direction), where d and $-d$ are known values that represent the designed bias and OV is the actual overlay error induced in the manufacturing processes. Therefore, the total overlay displacement in the two target gratings will be $OV + d$ and $OV - d$, respectively. By collecting the zeroth-order Mueller matrices associated with the two target gratings, and according to Eq. (S1), we will have

$$\Delta M_{+d} \approx K \cdot (OV + d) , \tag{S2a}$$

$$\Delta M_{-d} \approx K \cdot (OV - d) . \tag{S2b}$$

According to Eq. (S2), we can finally obtain the overlay error OV as

$$OV = \frac{\Delta M_{+d} + \Delta M_{-d}}{\Delta M_{+d} - \Delta M_{-d}} \cdot d . \tag{S3}$$

Note that the Mueller matrix elements in Eq. (S3) can be normalized or unnormalized to the M_{11} element.
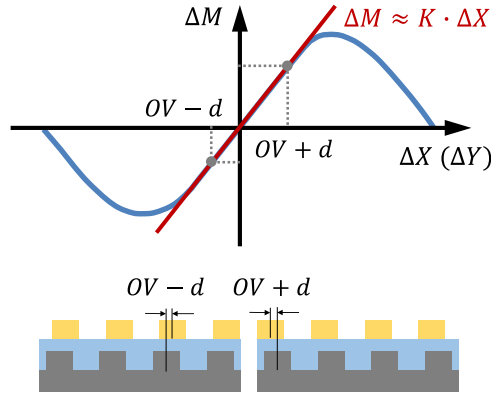

Fig.S1 Principle of the DBO metrology based on the zeroth-order Mueller matrix

2. Other configurations for the snapshot measurement of combinations of off-diagonal-block Mueller matrix elements

According to Eq. (1), by letting $\delta_1 = \delta_2 = \delta$ and adjusting the orientations of the polarization components, α_1, α_2, β_1, β_2, we can obtain some other configurations for the snapshot

measurement of combinations of off-diagonal-block Mueller matrix elements, as summarized in Table S1.

Table S1. Other configurations for the snapshot measurement of combinations of off-diagonal-block Mueller matrix elements

Configurations	Combinations of off-diagonal-block Mueller matrix elements	Associated frequency channels
$\alpha_1 = 0°$, $\beta_1 = \pm45°$, $\beta_2 = 0°$, $\alpha_2 = \mp45°$	$M_{41} - M_{14}$	$C_1(h)$
$\alpha_1 = 90°$, $\beta_1 = \pm45°$, $\beta_2 = 90°$, $\alpha_2 = \mp45°$	$M_{41} - M_{14}$	$C_1(h)$
$\alpha_1 = \pm45°$, $\beta_1 = 0°$, $\beta_2 = \mp45°$, $\alpha_2 = 0°$	$M_{41} - M_{14}$	$C_1(h)$
$\alpha_1 = \pm45°$, $\beta_1 = 90°$, $\beta_2 = \mp45°$, $\alpha_2 = 90°$	$M_{41} - M_{14}$	$C_1(h)$
$\alpha_1 = 0°$, $\beta_1 = \pm45°$, $\beta_2 = \pm45°$, $\alpha_2 = 0°$	$M_{41} - M_{14}$, $M_{42} - M_{24}$	$C_1(h)$, $C_2(h)$
$\alpha_1 = 90°$, $\beta_1 = \pm45°$, $\beta_2 = \pm45°$, $\alpha_2 = 90°$	$M_{41} - M_{14}$, $M_{42} - M_{24}$	$C_1(h)$, $C_2(h)$
$\alpha_1 = \pm45°$, $\beta_1 = 0°$, $\beta_2 = 0°$, $\alpha_2 = \pm45°$	$M_{13} + M_{31}$, $M_{41} - M_{14}$	$C_1(h)$
$\alpha_1 = \pm45°$, $\beta_1 = 90°$, $\beta_2 = 90°$, $\alpha_2 = \pm45°$	$M_{13} + M_{31}$, $M_{41} - M_{14}$	$C_1(h)$

3. Analysis in the presence of systematic errors

The measurement of the combination of the off-diagonal-block Mueller matrix elements $M_{13} + M_{31}$ or $M_{41} - M_{14}$ according to Eqs. (1)-(5) relies on the accurate alignment of orientations of the polarization components. Nevertheless, note that the measurement results are ultimately used for overlay metrology. According to Section 1 of this Supplement, the key of the DBO metrology based on the zeroth-order Mueller matrix lies in the linear relation between the combination of the off-diagonal-block Mueller matrix elements ΔM and the overlay error OV. Therefore, minor alignment errors in orientations of the polarization components could be acceptable, provided that the final measurement results of the combinations of the off-diagonal-block Mueller matrix elements do not affect the above linear relation in DBO metrology.

We analyze the measurement results of the combinations of the off-diagonal-block Mueller matrix elements in the presence of alignment errors. Considering that the alignment errors are typically small values, we adopt the following approximations in the analysis, i.e., $\sin\varepsilon \approx \varepsilon$, $\cos\varepsilon \approx 1 - \varepsilon^2/2$, and ignore high-order error terms. We denote the alignment errors in the orientations of the polarizer, the analyzer, and the two retarders as $\delta\alpha_1$, $\delta\alpha_1$, $\delta\beta_1$, and $\delta\beta_2$, respectively. In the presence of alignment errors, the system model given in Eq. (1) can be rewritten as

$$\mathbf{S}_{out} = \left[\mathbf{M}_A \mathbf{R}(\alpha_2 + \delta\alpha_2) \right] \cdot \left[\mathbf{R}(-\beta_2 - \delta\beta_2) \mathbf{M}_R(\delta_2) \mathbf{R}(\beta_2 + \delta\beta_2) \right] \cdot \mathbf{M}_S \cdot$$
$$\left[\mathbf{R}(-\beta_1 - \delta\beta_1) \mathbf{M}_R(\delta_1) \mathbf{R}(\beta_1 + \delta\beta_1) \right] \cdot \left[\mathbf{R}(-\alpha_1 - \delta\alpha_1) \mathbf{M}_P \right] \cdot \mathbf{S}_{in} . \tag{S4}$$

According to Eq. (S4), we have

$$I_{\text{out}} = \frac{1}{4} I_{\text{in}} \left\{ M_{11} + \frac{1}{2}(M_{33} - M_{44}) + 2(\delta\beta_1 - \delta\alpha_1)M_{12} + 2(\delta\beta_2 - \delta\alpha_2)M_{21} - \delta\beta_2 M_{23} - \delta\beta_1 M_{32} \right.$$

$$+ \frac{1}{2} \left[(M_{13} + M_{31}) - 2\delta\beta_1 M_{12} - 2\delta\beta_2 M_{21} + 2(\delta\beta_2 - \delta\alpha_2)M_{23} + 2(\delta\beta_1 - \delta\alpha_1)M_{32} \right.$$

$$\left. + i(M_{41} - M_{14}) - i2(\delta\beta_2 - \delta\alpha_2)M_{24} + i2(\delta\beta_1 - \delta\alpha_1)M_{42} \right] e^{i\delta}$$

$$+ \frac{1}{2} \left[(M_{13} + M_{31}) - 2\delta\beta_1 M_{12} - 2\delta\beta_2 M_{21} + 2(\delta\beta_2 - \delta\alpha_2)M_{23} + 2(\delta\beta_1 - \delta\alpha_1)M_{32} \right.$$

$$\left. - i(M_{41} - M_{14}) + i2(\delta\beta_2 - \delta\alpha_2)M_{24} - i2(\delta\beta_1 - \delta\alpha_1)M_{42} \right] e^{-i\delta}$$

$$+ \frac{1}{4} \left[(M_{33} + M_{44}) - 2\delta\beta_1 M_{32} - 2\delta\beta_2 M_{23} + i(M_{43} - M_{34}) + i2\delta\beta_2 M_{24} - i2\delta\beta_1 M_{42} \right] e^{i2\delta}$$

$$\left. + \frac{1}{4} \left[(M_{33} + M_{44}) - 2\delta\beta_1 M_{32} - 2\delta\beta_2 M_{23} - i(M_{43} - M_{34}) - i2\delta\beta_2 M_{24} + i2\delta\beta_1 M_{42} \right] e^{-i2\delta} \right\}$$

$$\tag{S5}$$

By taking the inverse Fourier transform of the channels in the OPD domain, we will have

$$\operatorname{Re}\left\{8\mathcal{F}^{-1}\{C_1(h)\}e^{-i\delta(\sigma)}\right\} / I_{\text{in}}(\sigma)$$
$$= M_{13} + M_{31} - 2\delta\beta_1 M_{12} - 2\delta\beta_2 M_{21} + 2(\delta\beta_2 - \delta\alpha_2)M_{23} + 2(\delta\beta_1 - \delta\alpha_1)M_{32} \tag{S6a}$$

$$\operatorname{Im}\left\{8\mathcal{F}^{-1}\{C_1(h)\}e^{-i\delta(\sigma)}\right\} / I_{\text{in}}(\sigma)$$
$$= M_{41} - M_{14} - 2(\delta\beta_2 - \delta\alpha_2)M_{24} + 2(\delta\beta_1 - \delta\alpha_1)M_{42} \tag{S6b}$$

As can be observed from Eq. (S6), in the presence of alignment errors, the real part of the channel $C_1(h)$ contains both the combination $M_{13} + M_{31}$ and the contributions from the elements M_{12}, M_{21}, M_{23}, and M_{32}. Meanwhile, the imaginary part of the channel $C_1(h)$ contains both the combination $M_{41} - M_{14}$ and the contributions from the elements M_{24} and M_{42}. In the absence of overlay errors, the off-diagonal-block Mueller matrix elements M_{23}, M_{32}, M_{24}, and M_{42} are equal to zero when the plane of incidence parallel to grating lines. However, the elements M_{12} and M_{21} are generally not equal to zero at any azimuthal configurations of the target grating, which will ultimately lead to a nonzero intercept in the linear relation for overlay metrology. From this aspect, the imaginary part the channel $C_1(h)$, i.e., Eq. (S6b), seems to be better than its counterpart, i.e., Eq. (S6a).

4. Relation between thicknesses of the multi-order retarders and spectral resolution of the detector

The multi-order retarders are critical components in the spectral polarization-coding technique. As schematically shown in Fig. 1, there are totally 5 frequency channels in the collected intensity spectrum. The frequency channels can be separated from each other by selecting proper thicknesses of the multi-order retarders. Generally, as the thickness of the multi-order retarder increases, the distance between adjacent frequency channels becomes larger, which is beneficial to avoid channel crosstalk. From another aspect, with the increase of the thickness of the multi-order retarder, the spectral resolution of the detector also needs to be improved in order to satisfy the well-known Nyquist-Shannon sample theorem. In other words, there should be a constraint relation between thicknesses of the multi-order retarders and spectral resolution of the detector.

To derive the above constraint relation, without loss of generality, we denote the thicknesses of the two multi-order retarders (R_1 and R_2 in Fig. 1) as t. We assume that the detector is a wavelength evenly sampling system (such as a spectrometer) with an effective spectral range

of $[\lambda_{\min}, \lambda_{\max}]$ and a spectral resolution of $\Delta\lambda$. Note that the following results can be readily adjusted to a wavenumber evenly sampling system (such as a Fourier transform spectrometer).

The number of sampling points of the collected intensity spectrum by the detector is $N = (\lambda_{\max} - \lambda_{\min})/\Delta\lambda$. The highest frequency of the channeled spectrum in the OPD domain can be expressed as

$$f_{\max} = 2B(\sigma)_{\max} \cdot t, \tag{S7}$$

where $B(\sigma)_{\max}$ represents the maximum birefringence of the multi-order retarders in the spectral range of $[\lambda_{\min}, \lambda_{\max}]$. Since the wavenumber resolution is not uniform at both ends of the spectrum, we use the geometric mean

$$\Delta\sigma \approx \sqrt{\Delta\sigma_{\min} \cdot \Delta\sigma_{\max}} = \frac{\Delta\lambda}{\lambda_{\max} \cdot \lambda_{\min}} \tag{S8}$$

as the resolution of the spectrum in the wavenumber domain. Hence, the sampling frequency of the spectrum in the OPD domain is

$$f_s = \frac{1}{\Delta\sigma}. \tag{S9}$$

According to the sampling theorem ($f_s > 2f_{\max}$), the minimum number of sampling points required for the detector can be calculated as

$$N > \frac{4B(\sigma)_{\max} t(\lambda_{\max} - \lambda_{\min})}{\lambda_{\max} \cdot \lambda_{\min}}. \tag{S10}$$

For the multi-order retarders made of MgF$_2$ with thicknesses of $t = 6.4$ mm, according to Eq. (S10), we can know that the minimum number of sampling points is $N = 374$ for a detector with an effective spectral range of 400~800 nm. In other words, the spectral resolution of the detector should be higher than 1.07 nm.
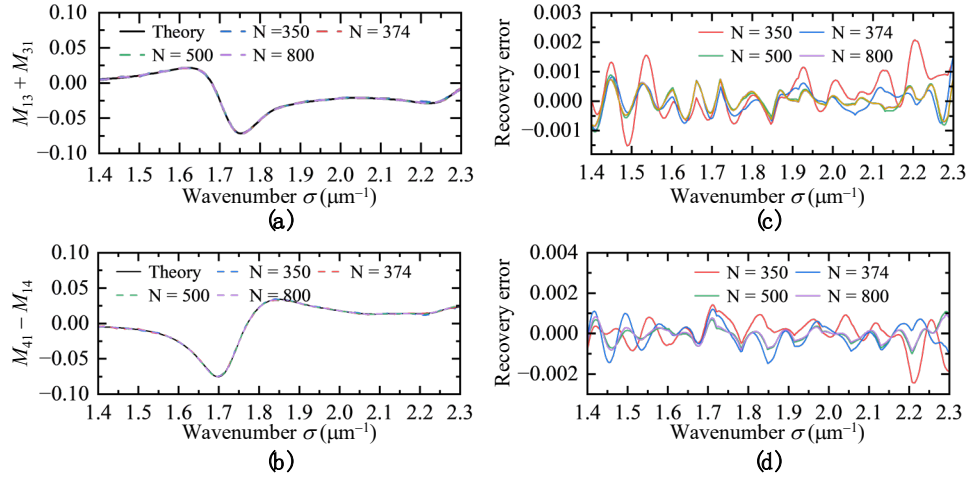

Fig.S2 Recovery results of (a) $M_{13} + M_{31}$ and (b) $M_{41} - M_{14}$ with different numbers of sampling points $N = 350, 374, 500,$ and 800, respectively, (c) and (d) the corresponding recovery errors to (a) and (b), respectively. The $M_{13} + M_{31}$ and $M_{41} - M_{14}$ spectra were calculated for the $OV - d$ target grating at the incidence angle of $\theta = 65°$ and azimuthal angle of $\phi = 90°$.

Figure S2 presents the recovery results of $M_{13} + M_{31}$ and $M_{41} - M_{14}$ with the number of sampling points $N = 350, 674, 500,$ and 800, respectively. As can be observed, although $M_{13} + M_{31}$ and $M_{41} - M_{14}$ can be recovered when $N = 350$, the recovery errors at some wavelengths are relatively large due to the under-sampling rate. In comparison, a better recovery performance can be achieved when $N \geq 374$. Moreover, with the increase of the number of sampling points, the recovery accuracy can be increased to a certain extent. The residual recovery errors are attributed to the random noise in the intensity spectrum, the recovery algorithm, as well as the actual nonlinear dispersion of the retardance of MgF_2.

5. Other simulation results

Figure S3 presents the comparison between the recovered and the RCWA-calculated theoretical spectra of $M_{13} + M_{31}$ and $M_{41} - M_{14}$ for the two target gratings ($OV + d$ and $OV - d$) at the incidence angle of $\theta = 65°$ and azimuthal angle of $\phi = 75°$. Figure S4 presents the comparison between the preset (input) and the measured overlay errors from the recovered $M_{13} + M_{31}$ and $M_{41} - M_{14}$ spectra at $\theta = 65°$ and $\phi = 75°$. The values of $M_{13} + M_{31}$ and $M_{41} - M_{14}$ were first averaged over the spectral range from about 500 nm to 550 nm, respectively, and then used to measure overlay errors.
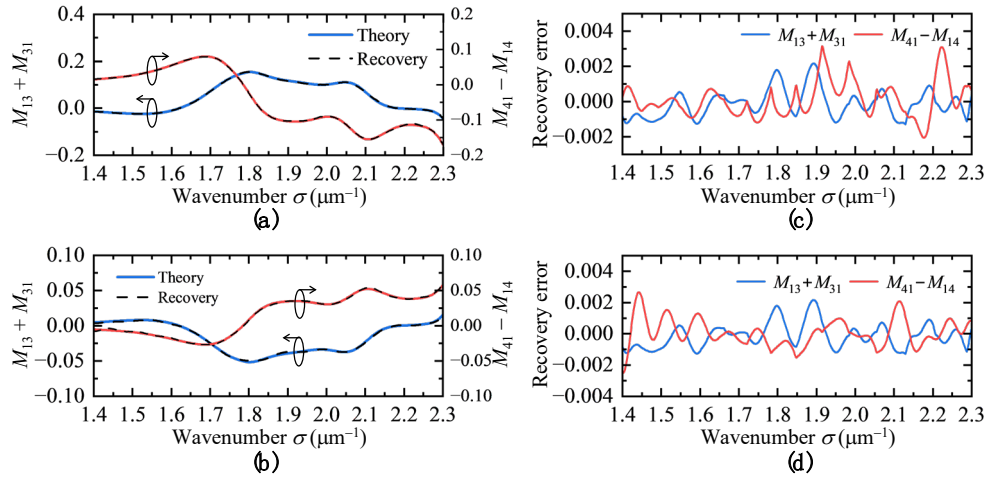

Fig.S3 Comparison between the theoretical and recovered spectra of $M_{13} + M_{31}$ and $M_{41} - M_{14}$ for the two target gratings: (a) $OV + d$ and (b) $OV - d$ at the incidence angle of $\theta = 65°$ and azimuthal angle of $\phi = 75°$, where the overlay error was set to be $OV = 5$ nm; (c) and (d) the corresponding recovery errors.
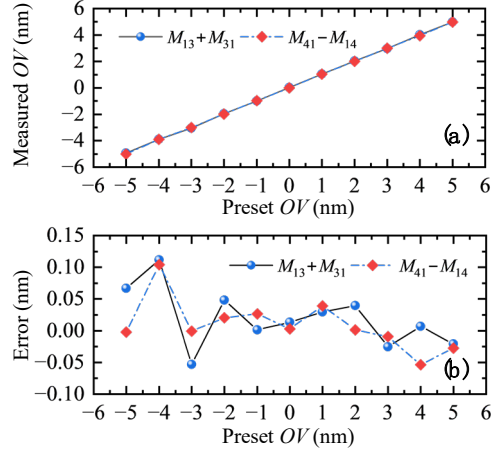
Fig.S4 (a) Comparison between the preset and measured overlay errors from the $M_{13} + M_{31}$ and $M_{41} - M_{14}$ spectra collected at the incidence angle of $\theta = 65°$ and azimuthal angle of $\phi = 75°$, (b) the corresponding measurement errors.

Figure S5 presents the comparison between the preset (input) and the measured overlay errors from the recovered $M_{13} + M_{31}$ and $M_{41} - M_{14}$ at $\theta = 65°$, $\phi = 75°$, and at the wavelengths of $\lambda = 500$ nm and $\lambda = 550$ nm, respectively. The comparison between Figs. 4 and S5 demonstrates that multi-wavelength averaging yields higher accuracy than single wavelength in overlay measurement, since multi-wavelength averaging reduces errors induced by random noise and recovery errors in the recovered $M_{13} + M_{31}$ and $M_{41} - M_{14}$.
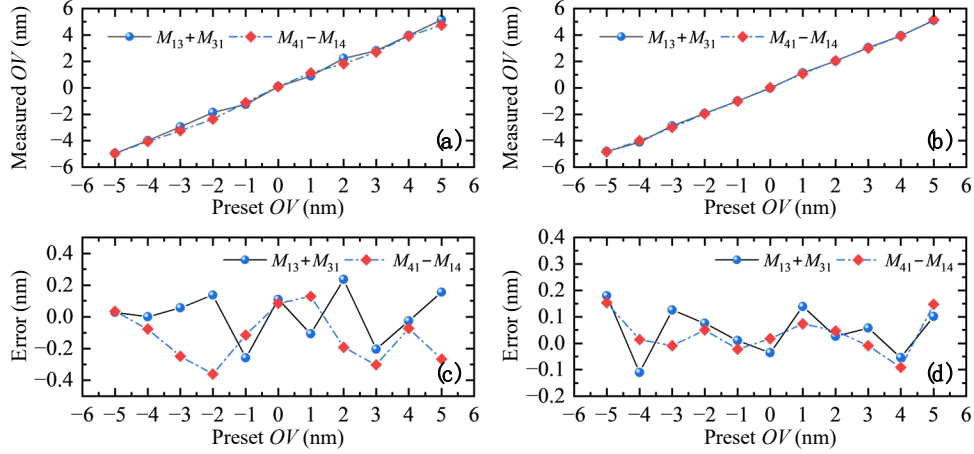

Fig.S5 Comparison between the preset and measured overlay errors from the $M_{13} + M_{31}$ and $M_{41} - M_{14}$ collected at the wavelengths of (a) $\lambda = 500$ nm and (b) $\lambda = 550$ nm and at the incidence angle of $\theta = 65°$ and azimuthal angle of $\phi = 90°$; (c) and (d) the corresponding measurement errors.